GEOLOGY

First source-to-sink monitoring shows dense head controls sediment flux and runout in turbidity currents

Ed L. Pope[1]*, Matthieu J. B. Cartigny[1], Michael A. Clare[2], Peter J. Talling[3], D. Gwyn Lintern[4], Age Vellinga[2,5], Sophie Hage[6,7], Sanem Açikalin[8], Lewis Bailey[2,5], Natasha Chapplow[9], Ye Chen[10], Joris T. Eggenhuisen[11], Alison Hendry[8], Catharina J. Heerema[9,12], Maarten S. Heijnen[2,5], Stephen M. Hubbard[7], James E. Hunt[2], Claire McGhee[8], Daniel R. Parsons[10], Stephen M. Simmons[10], Cooper D. Stacey[4], Daniela Vendettuoli[2,5]

Until recently, despite being one of the most important sediment transport phenomena on Earth, few direct measurements of turbidity currents existed. Consequently, their structure and evolution were poorly understood, particularly whether they are dense or dilute. Here, we analyze the largest number of turbidity currents monitored to date from source to sink. We show sediment transport and internal flow characteristic evolution as they runout. Observed frontal regions (heads) are fast (>1.5 m/s), thin (<10 m), dense (depth averaged concentrations up to 38%$_{vol}$), strongly stratified, and dominated by grain-to-grain interactions, or slower (<1 m/s), dilute (<0.01%$_{vol}$), and well mixed with turbulence supporting sediment. Between these end-members, a transitional flow head exists. Flow bodies are typically thick, slow, dilute, and well mixed. Flows with dense heads stretch and bulk up with dense heads transporting up to 1000 times more sediment than the dilute body. Dense heads can therefore control turbidity current sediment transport and runout into the deep sea.

INTRODUCTION

Turbidity currents are underwater sediment-laden flows that move downslope because of their excess density (1). These flows are globally important in terms of sediment (2), nutrient (3), pollutant (4), and organic carbon (5, 6) transport from rivers and coasts to the deep sea. They also pose a major hazard to subsea infrastructure (7), including seafloor telecommunication cables, which carry >99% of intercontinental data traffic globally (8). However, no measurements of these flows yet exist from source to sink, and we are therefore yet to constrain how flows move sediment through a submarine channel system. For example, we have not constrained (i) how flow frequency changes along a system, particularly in modern systems (9, 10); or (ii) whether flows are entirely dilute and fully turbulent sediment suspensions or contain dense near-bed layers that dominate sediment flux, flow evolution, and runout; or (iii) whether flows evolve in a common manner from initiation to termination. These uncertainties relate to a lack of field measurements of modern flows. We therefore rely on interpreting flow characteristics from deposits alone [which are typically highly incomplete due to the effects of erosion by successive flows (9–11)] or scaled relationships from laboratory experiments. This reliance on ancient deposits or scaled-down experiments inhibits robust field-scale quantification

of fundamental properties, such as the volume of sediment transported by individual flows through a system (12, 13) and the physical processes that govern the flows themselves, such as the mechanism(s) by which sediment is supported (i.e., whether grain-to-grain interactions or turbulence dominates) (1, 14–20). Observations and analyses of a large number of turbidity currents from start to finish are therefore critical to determine the range of flow behaviors that exist, and how flows evolve as they move downslope. Here, we address a key open question: whether dilute or dense sediment suspensions dominate sediment and organic carbon transfer and runout. The physics of dense and dilute flows are very different (21); until we know the fundamental character of real-world flows, it is not feasible to predict their behavior and runout, or to quantify deep-sea sediment fluxes, design resilient seafloor infrastructure routes, and determine their role in organic carbon cycling in the ocean.

The first studies to directly monitor turbidity currents using acoustic Doppler current profilers (ADCPs) suggest that these flows can develop fast, dense heads that drive the flow (2, 22–24). The velocity differential between the head and the body can result in flow stretching (23). The greater erosive potential of higher-velocity (>4 m s^{-1}) heads may also make ignition, a process by which a faster head is able to erode more material and thus become denser and faster, more likely enabling longer runout (25, 26). However, slow flows of shorter duration have also been observed in action (24, 27, 28). These different observed characteristics suggest that flows are able to erode and bulk up (increase the sediment mass being transported by the flow) as long as they remain above a threshold velocity and basal shear stress (26, 29). Below this threshold velocity, the head rapidly decelerates, before the flow slows and becomes dilute (25). This model remains untested at field scale as most previous monitoring studies were limited to a small number of flows ($N \approx 10$) recorded at individual mooring locations (22–24, 27). Alternatively, where flows have been monitored at multiple locations along a channel, the instruments are largely restricted to parts of the system proximal to the coast, the number of observed flows is

[1]Department of Geography, Durham University, Science Laboratories, South Road, Durham DH1 3LE, UK. [2]National Oceanography Centre Southampton, European Way, Southampton SO14 3ZH, UK. [3]Departments of Earth Science and Geography, Durham University, Science Laboratories, South Road, Durham DH1 3LE, UK. [4]Geological Survey of Canada, Natural Resources Canada, 9860 W Saanich Road, Sidney, BC V8L 4B2, Canada. [5]School of Ocean and Earth Sciences, University of Southampton, European Way, Southampton SO14 3ZH, UK. [6]Univ Brest, CNRS, Ifremer, Geo-Ocean, F-29280 Plouzané, France. [7]Department of Geoscience, University of Calgary, Calgary, AB T2N 1N4, Canada. [8]School of Civil Engineering and Geosciences, Newcastle University, Newcastle upon Tyne NE1 7RU, UK. [9]Department of Earth Science, Durham University, Science Laboratories, South Road, Durham DH1 3LE, UK. [10]Energy and Environment Institute, University of Hull, Hull HU6 7RX, UK. [11]Faculty of Geosciences, Utrecht University, P.O. Box 80021, 3508 TA Utrecht, Netherlands. [12]Department of Geography, University of Victoria, Victoria, BC V8W 2Y2, Canada.
*Corresponding author. Email: edward.pope@durham.ac.uk

small ($N \leq 15$), and key characteristics, such as sediment concentration, that drive the flow have not been measured or derived (*2*, *26*, *30*). It has therefore not been possible to develop a model that robustly captures the full range of turbidity current characteristics and how or why flows may evolve from one set of characteristics to another.

Here, we document 95 turbidity currents along a 40-km-long submarine channel-lobe system from source to sink in Bute Inlet, Canada. We directly measured flow velocity, flow height, and duration using six ADCPs moored at locations from the Homathko Delta down to a terminal channel lobe (Fig. 1). These measurements are
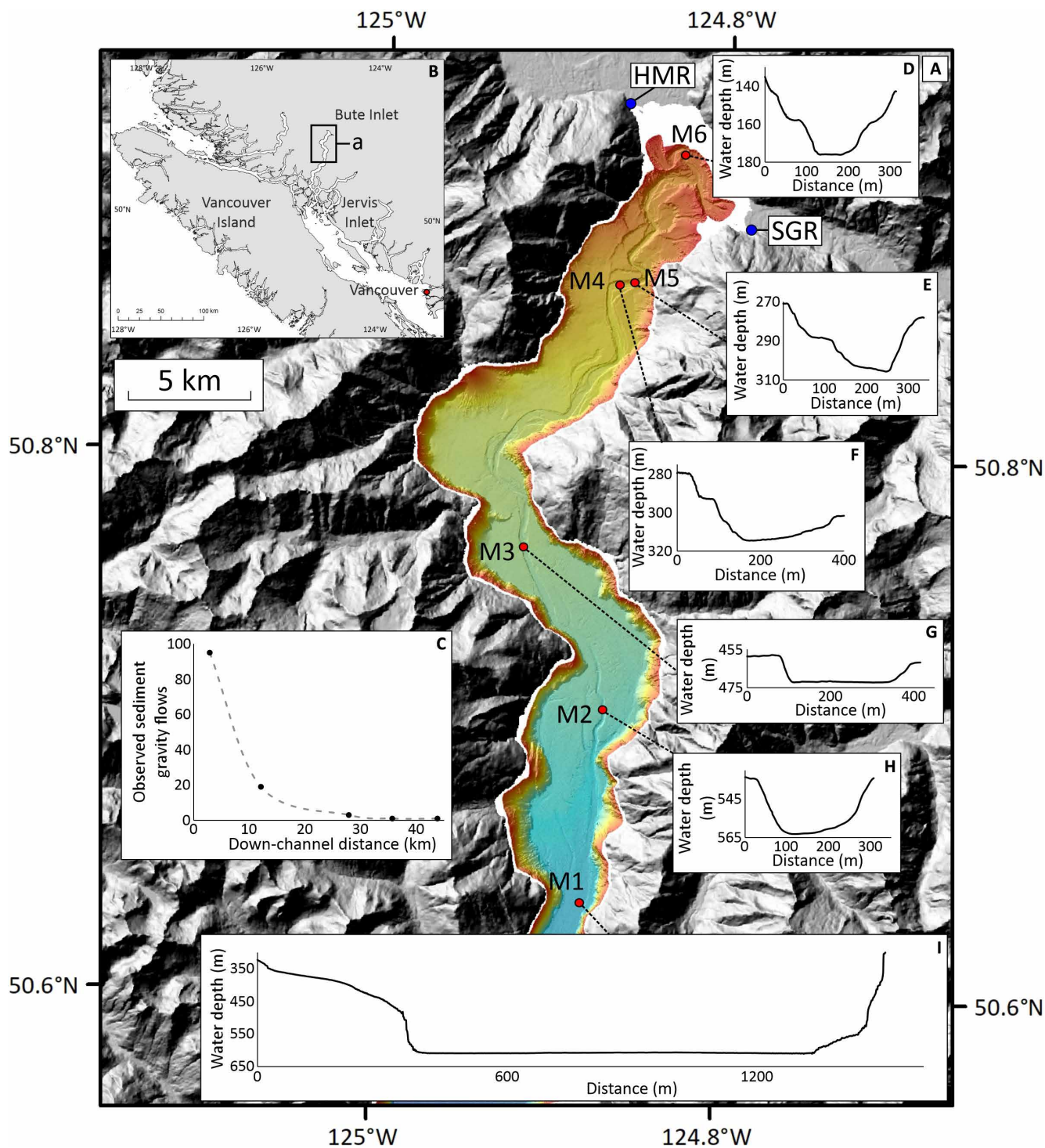
Fig. 1. Mooring locations in Bute Inlet. (**A**) Bathymetric map of the channel in Bute Inlet with instrument mooring locations (M6 to M1). HMR, Homathko River Mouth; SGR, Southgate River Mouth. (**B**) Inset map shows the location of Bute Inlet in British Columbia, Canada. (**C**) Observed number of turbidity currents at each mooring triggered from the Homathko Delta. (**D** to **I**) Channel cross sections at each mooring location.

used to derive other key characteristics that control turbidity current behavior using a modified Chézy approach (*31*, *32*). These derived characteristics are depth-averaged sediment concentrations, bulk Richardson numbers (*Ri*; i.e., the amount of turbulence), and the ratio between bed friction (C_{fb}) and the friction between the flow and the ambient water (C_{fi}). The Chézy approach is commonly used in rivers to model open channel flow, but it has also been applied to the study of turbidity currents and balances local driving and resistive forces. It assumes no inherited momentum from upslope, such that the flow is a perfect balance of the driving and frictional forces at the point of measurement (see Materials and Methods) (*33–35*). The Chézy method generates single depth-averaged values for parameters that vary with height in the flow, for example, sediment concentrations will probably be higher close to the bed. Using this unusually detailed ADCP dataset, with the largest number of flows yet observed, we document how turbidity current characteristics change as they move past a mooring and how these characteristics change as the flow evolves down-system, from source to deep-sea sink. On the basis of these characteristics, we define three distinct flow types. Within these flow types, we show which flow regimes (i.e., dense or dilute) dominate sediment transport rates, how flow regimes are distributed within a flow, and how dense and dilute layers control flow behavior. Dense heads at the front of the flows are shown to carry up to 1000 times more sediment than the much longer subsequent dilute body of these flows. Flows are also shown to bulk up (erode and entrain sediment) by up to three orders of magnitude as they move down-channel. These derived sediment masses are then compared with predictions of sediment transport from commonly used models (*36–38*).

Bute Inlet channel system
Bute Inlet is a fjord in British Columbia, Canada, that lies in the Pacific Range of the Coastal Mountains (Fig. 1). The head of the inlet is fed by freshwater and sediment delivered by the Homathko and Southgate Rivers, of which the Homathko supplies ~80% of the freshwater input (*39*, *40*). The Homathko sediment load is composed of 15% gravel, 65% sand, 15% silt, and 5% clay (*41*). However, it can also introduce organic debris, trees, and branches when in flood (*40*). A 50-km-long submarine channel-lobe system (Fig. 1) extends from the prodeltas of the two rivers to a terminal lobe at 650-m water depth. The channel floor is composed mainly of fine to coarse sand, while the overbanks areas are dominated by silt and mud (*6*). Turbidity currents within this system occur predominantly during the summer freshet, when Homathko River discharge increases as a result of increased glacier and snow melt (*39*, *40*). The positioning of ADCP-mooring M6 (Fig. 1) above the confluence of the Homathko and Southgate Channel tributaries means this study will focus on turbidity currents triggered from the Homathko Delta (see the Supplementary Materials for more details).

RESULTS
The ADCP array recorded 95 turbidity currents sourced from the Homathko Delta at the shallowest mooring (M6; Table 1, table S3, and Fig. 1C) between May and November 2018. Only 19 flows were observed at the next mooring (M4; 12 km down-channel; Fig. 1A). A single flow traversed the entire ADCP array to the deepest mooring just downstream of the end of the channel (M1; 43.8 km down-channel; Fig. 1). Turbidity currents were flowing past M6 during 4% of the

monitoring period. This was reduced to 3% at M4, 0.7% at M3, and 0.5% at M2 and M1.

The ADCP measurements show that these turbidity currents are divided into three general types (Fig. 2). Type 1 flows have fast and thin heads and are the least common (*N* = 11 at M6; Fig. 2A and Table 1). Behind these heads, the flows thickened rapidly while velocities decayed (Fig. 2). These flows had the greatest measured internal velocities (max = 6.2 m s^{-1}; average = 3.7 m s^{-1}), durations (average = 3.4 hours), and total displaced fluid volumes (average = 0.008 km^3 mixture of water and sediment) when averaged across all flows of this type.

Type 2 flows (*N* = 30 at M6) were identified by an initially thin head, which lacked the high-velocity core of type 1 flows (Fig. 2B). Behind the head, type 2 flows rapidly thickened and commonly had a higher-velocity core at the base of the flow. The average of the maximum measured velocities of these flows at M6 was 1.5 m s^{-1} (Table 1). These flows also had an average duration of 2.6 hours and an average total displaced volume of 0.006 km^3.

Type 3 flows were the most common (*N* = 54 at M6), being characterized by the lowest measured maximum velocities (0.7 m s^{-1}; Fig. 2C and Table 1). These flows lacked any high-velocity regions and were comparable to the lower-velocity body and tails of the other flow types. These flows had the shortest average durations (1.9 hours) and lowest average displaced volumes (0.003 km^3).

ADCP-measured velocities show turbidity currents with higher initial velocities (i.e., measured close to their source) tend to runout further (fig. S1). The longest runout flows had the greatest ADCP-measured velocity at the upstream mooring (M6) and were therefore most likely to reach M4 (12 km down-channel). Of the 15 flows with measured velocities >2 m s^{-1} at M6, all but one reached M4. At M4, the three flows with the fastest measured velocities (>3 m s^{-1}) ran out as far as M3 (27.9 km down-channel). At M4, the maximum flow velocities, durations, and displaced volumes remained greatest for flows with type 1 characteristics (3.2 m s^{-1}, 11.3 hours, 0.02 km^3; Fig. 2A) compared with those with type 2 characteristics (1.2 m s^{-1}, 10.1 hours, 0.02 km^3; Fig. 2B) or type 3 characteristics (0.7 m s^{-1}, 4.2 hours, 0.006 km^3). However, the durations and displaced volumes increased for all but two flows from M6 to M4 (flows 12 and 88; table S3). The duration and displaced volume of the flow recorded at M1 (i.e., at the terminal lobe) were 26.9 hours and 0.17 km^3, respectively.

Depth-averaged flow characteristics from the Chézy method
Depth-average characteristics inferred via the Chézy method are now reported. We first plot the frequency of measured depth-averaged velocities (*U*) for all flows at all moorings relative to normalized flow durations (Fig. 3A). Other derived properties, such as sediment concentration or flow thickness, are plotted as the third variable (shown in color) relative to *U* in the other panels (Fig. 3, B to E).

Most observed flows are entirely dilute (<0.01%$_{vol}$) and have thick (≥10 m), low-velocity (<0.5 m s^{-1}), and well-mixed (*Ri* < 0.25) heads. Friction during these flows is greater between the flow and the ambient water than with the bed ($C_{fb} < C_{fi}$). The body and tails of these flows are also dilute (Fig. 3). We refer to these characteristics as the dilute regime. Type 3 flows described above are entirely characterized by this regime.

A smaller proportion of flows have heads that are thin (<10 m; Fig. 3C), high velocity (up to 3.8 m s^{-1} depth-averaged velocity; Fig. 3A), and dense (up to 38%$_{vol}$; Fig. 3B), with suppressed or no mixing (*Ri* > 0.25). The heads of these flows experience greater

Table 1. Average properties of turbidity current types observed at each mooring during the 2018 Bute Inlet deployment. All flows are detailed in table S3.

	Flow type	Maximum ADCP velocity (m/s)	Duration (hours)	Water volume displaced (km^3)	Maximum sediment discharge (kg/s)	Sediment volume displaced (metric tons)
M6 Flows						
Mean	All Flows	1.33	2.27	0.0046	2064	690
Mean	Type 1	3.72	3.43	0.008	16,014	5293
Mean	Type 2	1.51	2.59	0.005	646	214
Mean	Type 3	0.79	1.89	0.003	26	26
M4 Flows						
Mean	All Flows	1.56	8.85	0.0172	20,689	28,649
Mean	Type 1	3.17	11.28	0.025	77,783	100,034
Mean	Type 2	1.17	10.08	0.019	445	4763
Mean	Type 3	0.66	4.20	0.006	35	256
M3 Flows						
Mean	All Flows	2.16	12.60	0.0260	92,338	221,375
Mean	Type 1	5.08	24.35	0.061	276,015	663,095
Mean	Type 2					
Mean	Type 3	0.70	6.73	0.008	500	516
M2 Flows						
Mean	All Flows	4.20	26.18	0.0582	12,734	24,792
Mean	Type 1	4.20	26.18	0.0582	12,734	24,792
Mean	Type 2					
Mean	Type 3					
M1 Flows						
Mean	All Flows	1.11	26.91	0.1679	804	6819
Mean	Type 1					
Mean	Type 2	1.11	26.91	0.1679	804	6819
Mean	Type 3					

friction at the bed than with the ambient water ($C_{fb} > C_{fi}$). We refer to these characteristics as the dense regime. In contrast, the body and tails of these flows are entirely dilute, well mixed ($Ri < 0.25$), and dominated by friction at the ambient water interface ($C_{fb} > C_{fi}$). These flows, equivalent to type 1 flows described above, therefore evolve from a dense regime head to a dilute regime body and tail.

Between these end-members, flow heads are characterized by moderate velocities (0.5 to 2.3 m s^{-1}; Fig. 3A), thicknesses, and densities, which are well mixed ($Ri \leq 0.25$), indicating that an intermediate or transitional regime exists. Friction during the heads of these flows is generally greater between the flow and the ambient water ($C_{fb} < C_{fi}$) but can be near parity where higher-velocity cores are present. These flows are equivalent to type 2 flows described above.

Sediment fluxes and total mass transported

Chézy-derived depth-averaged sediment concentrations were used to estimate the total mass of sediment transported past each mooring (Table 1; see Materials and Methods), as well as by the different flow regimes (Fig. 4). The sediment mass transported past a mooring by an individual flow varied by over six orders of magnitude: from 0.4 to 663,000 metric tons. The mass of sediment transported

past each mooring by the individual flow types thus varied by over six orders of magnitude. Type 1 flows transported orders of magnitude more sediment (486 to 33,684 metric tons at M6) than type 2 flows (23 to 141 metric tons at M6; see table S3), while type 2 flows carried more sediment than type 3 flows (0.363 to 82 metric tons at M6).

The mass of transported sediment also varied by orders of magnitude within individual flows according to the flow regimes in operation. Where flows feature fast, dense heads dominated by bottom friction ($C_{fb} > C_{fi}$), the duration of the head is considerably shorter than the dilute body and tail (fig. S4). However, despite its shorter duration, the mass of sediment transported by the dense regime head is generally much greater than in the body and tail (Fig. 4). Our data also show that as flows with fast, dense heads traverse the mooring array, the head of the flow bulks up through erosion; however, instead of changing its density, the head stretches. In contrast, the dilute regime parts of these flows also stretch, but the increase in displaced sediment mass contained within them is considerably smaller (Fig. 4).

Down-channel flow bulking (increases in transported sediment) is indicated by changes in the total mass of sediment displaced at each mooring. At M6, 95 flows displaced a total of 0.065 metric tons of sediment. This increased by an order of magnitude at M4
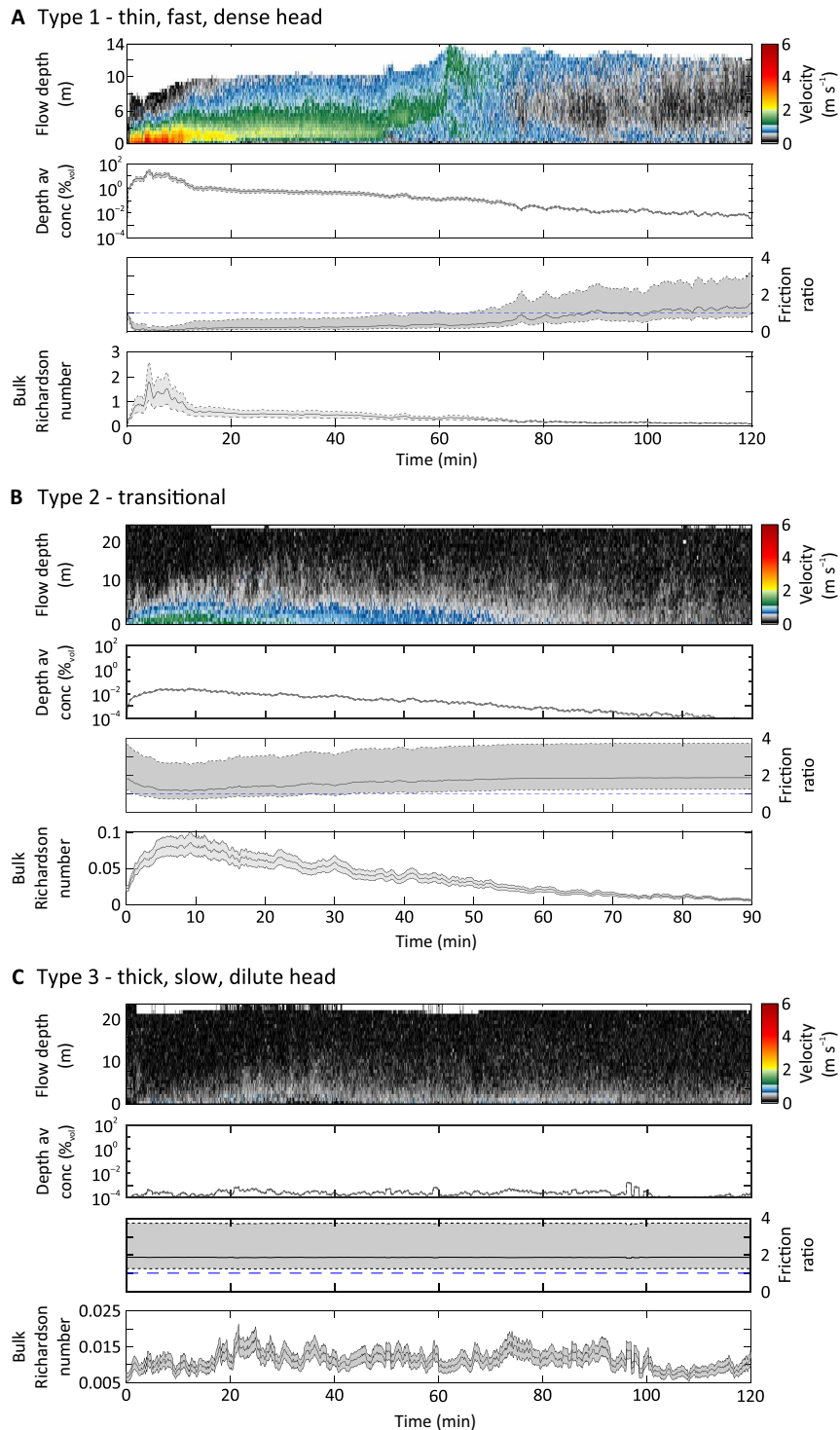
Fig. 2. Example velocity structures and Chézy-derived properties for different types of turbidity currents in Bute Inlet. The gray zones on the depth average (av) concentration, friction ratio, and bulk Richardson number plots indicate the range of properties that were derived by setting the bed friction between 0.002 and 0.006. (**A**) Type 1 turbidity current characterized by a thin, fast, and dense head with little mixing. (**B**) Type 2 turbidity current in a transitional state. (**C**) Type 3 turbidity current characterized as dilute with low velocities and large amounts of mixing occurring.
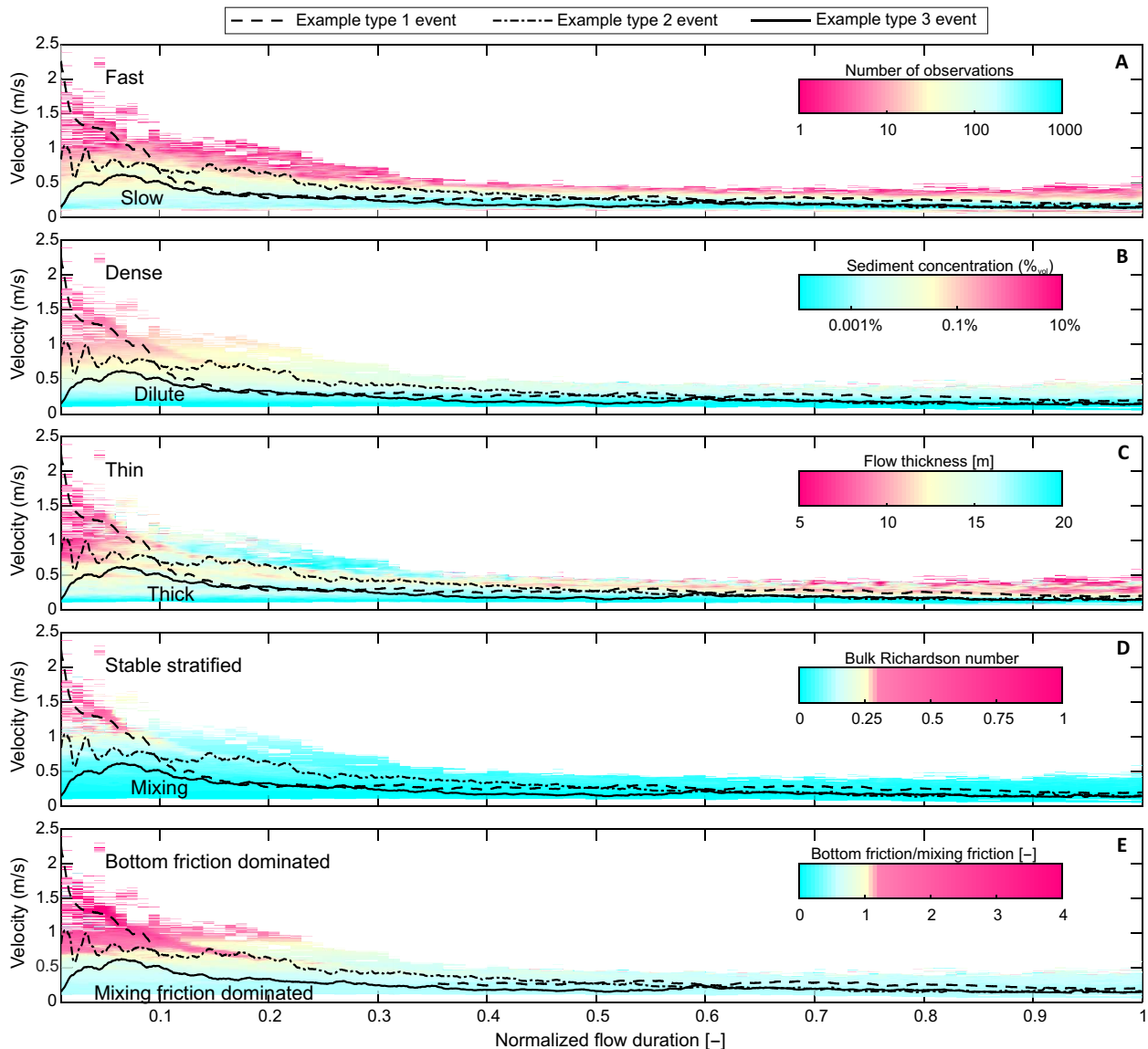
Fig. 3. Turbidity current characteristics derived from iteratively solved modified Chézy equations. Turbidity currents are commonly observed to be slow, dilute, thick, and strongly mixing flows (in blue) and uncommonly observed to be fast, dense, thin, and stably stratified flows (in pink). (**A**) Observed depth-averaged velocities of all turbidity currents. Depth-averaged velocity profiles are also displayed for characteristic examples of each flow type. (**B** to **E**) Chézy-derived variables plotted according to the observed depth-averaged velocities. (B) Flow concentrations are shown to increase with velocity. (C) High-velocity heads are shown to be thin compared with slower-moving flows. (D) High-velocity heads are shown to be stably stratified, while other parts of the flow are experiencing mixing. (E) Friction at the bed (C_{fb}) is greater than friction at the interface between the top of the flow and the ambient water (C_{fi}) in the high-velocity heads. The reverse is true for the majority of the flows.

(0.544 megatons) and M3 (0.664 metric tons) despite the marked decrease in the number of flows reaching each mooring (19 and 3, respectively). Total transported mass decreased to 0.025 and 0.007 metric tons at M2 and M1, respectively, as the longest runout flow began to wane.

DISCUSSION
Sediment fluxes and flow mass budgets
Our results have implications for understanding the reworking, deposition, and burial of sediment, organic carbon, and pollutants

in submarine channel systems. Most flows transport comparatively small volumes of sediment in shallow water depths in the proximal channel close to the river mouth (Fig. 1). Sediment transport further downstream is dominated by less frequent flows, which had initiated with and continue to sustain dense regime heads (type 1 flows). The down-channel bulking suggests that sediment entrainment via seabed erosion is a more important control on the total mass of sediment transported by a flow through a system than the initial mass of released sediment when the flow is triggered. However, the initial volume and nature of released material at the flow source likely govern the starting head density and hence also increase the potential for
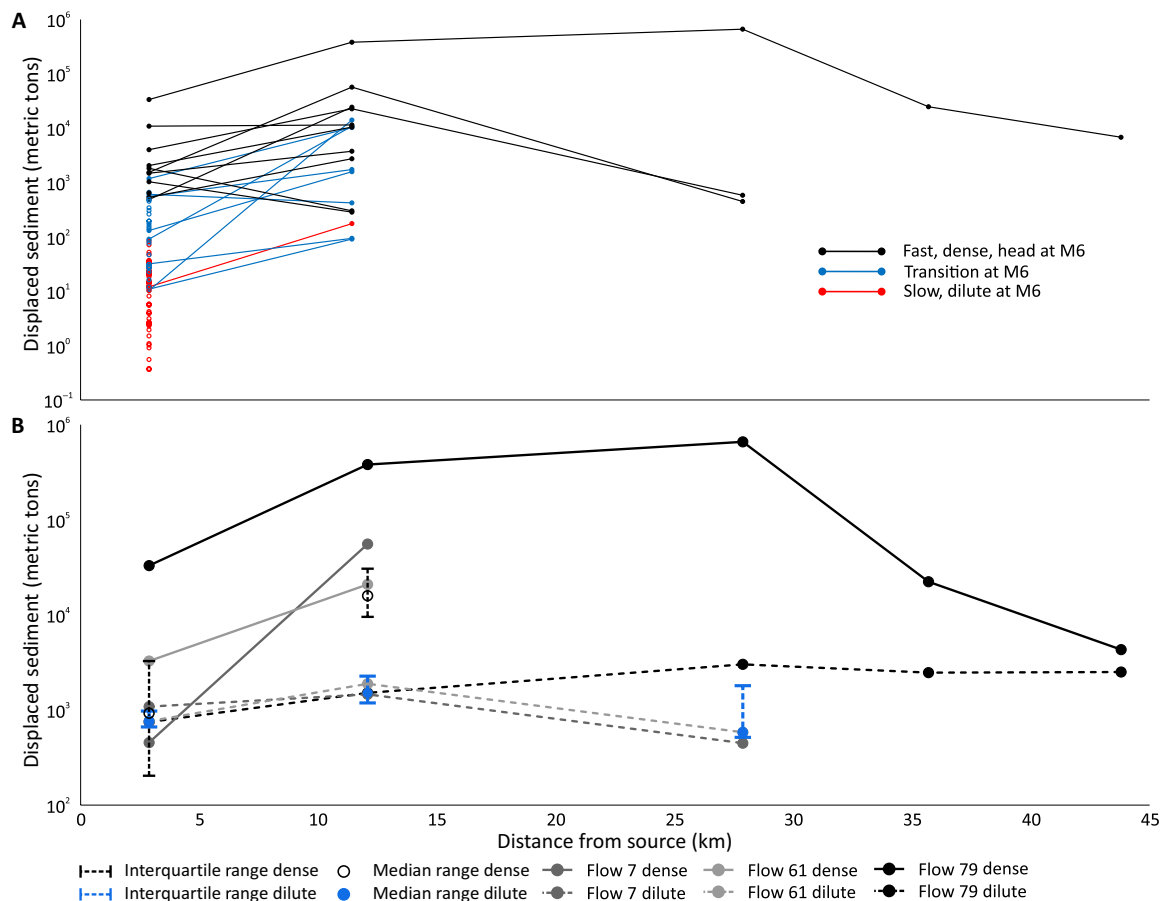
Fig. 4. Sediment mass-budgets for observed flows. (**A**) Sediment displaced by turbidity currents in Bute Inlet relative to their structure type at M6. Calculated displaced sediment based on iteratively solved Chézy equations assuming a bed friction coefficient (C_{fb}) of 0.004. (**B**) Sediment mass transported by fast and dense turbidity current heads, and the slow dilute bodies and tails as flows characterized by the presence of a fast, dense head at M6 moved through the mooring array (M6 to M1). Parts of the flow are categorized as "dense," where $C_{fb} > C_{fi}$, and "dilute," where $C_{fb} < C_{fi}$. The fast dense heads are shown to transport the majority of the sediment transported by individual turbidity currents despite the shorter duration when compared to the body and tail (see also fig. S5). All three flows that ran out as far as M3 are individually displayed.

erosion and resultant flow ignition (*2*). Material deposited by shorter runout flows will therefore likely be reworked, perhaps on multiple occasions before final burial.

The Homathko River delivers ~4 megatons of sediment annually to Bute Inlet, which is deposited on the pro-delta or settles out from suspension from the water column (*42*). The observed turbidity currents in 2018 only reworked a small fraction of this from the delta in the upper sections of the channel (~2% at M6). A notable fraction of the annual sediment input therefore appears to have been stored on the delta front or in the head of the submarine channel system. Some of this sediment will have been reworked by turbidity currents, which did not make it to M6, or short runout delta-lip collapses as have been observed on pro-deltas in similar settings such as Squamish (*43*). Less-frequent, larger-magnitude events that are capable of flushing sediment through this system to the lobe may occur but have not yet been observed.

Derived sediment fluxes and sediment transport models
Here, we compare changes in sediment transport inferred for turbidity currents based on our field observations and the Chézy approach, with models commonly used to predict sediment transport

(*36–38*). The aim was to determine whether both methods give consistent results, but this comparison more fundamentally illustrates how the exact choice of sediment erosion or transport model can give results that vary by orders of magnitude, hampering such a comparison. Sediment erosion here is modeled using the classic and commonly used model of Garcia and Parker (*36*) as well as a more recent model that is modified to adjust for high flow velocities and high erosion rates (*38*). Sediment deposition is modeled following Garcia (*37*), which is commonly used in combination with Garcia and Parker (*36*). Details on the models, and assumed constants, are detailed in Materials and Methods.

Figure 5 shows the predicted down-channel evolution of the volume of sediment within the longest runout flow (Flow 79; table S3) according to the different erosion and sediment transport models that were used compared to the field observations. Overall, the predicted changes in the sediment volume within the flow are a delicate balance between much larger predicted erosional and depositional fluxes. The results show how small changes in the assumptions that feed into these models will have large impacts on the predicted erosional and depositional fluxes and easily result in an order of magnitude over or under prediction of sediment within the flow. Such
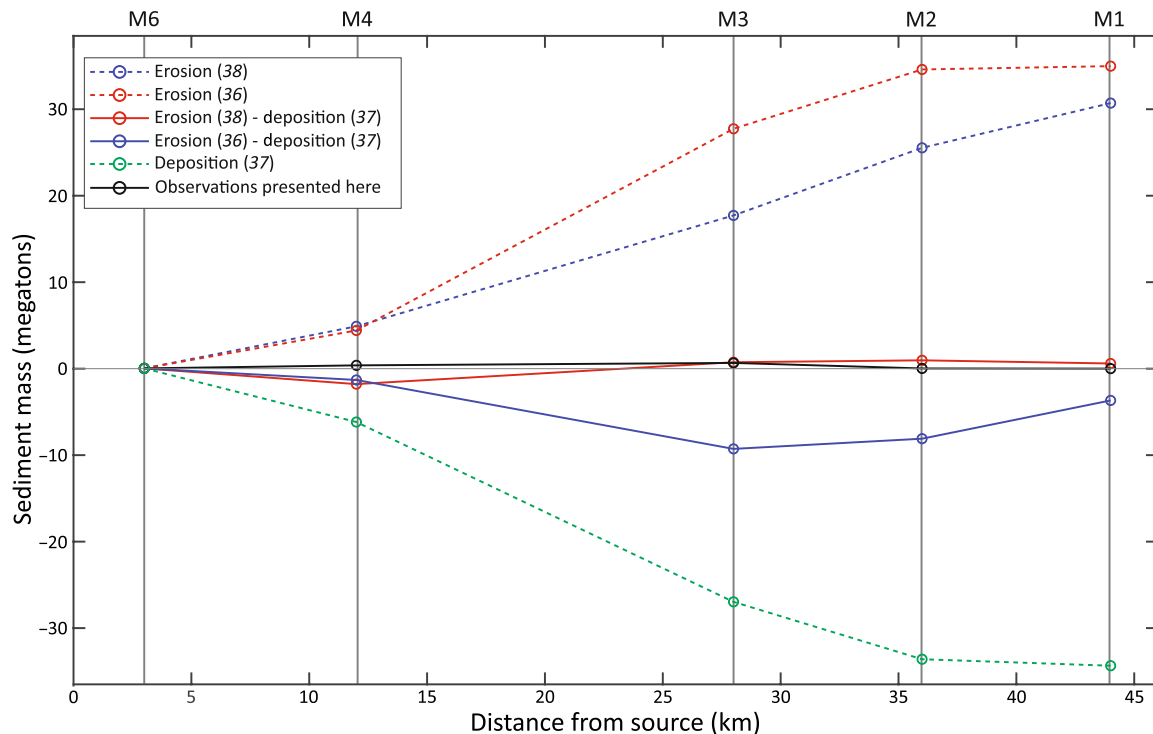
Fig. 5. Comparison of turbidity current sediment transport observations and models. The predicted and observed down-channel evolution of the mass of sediment within the longest runout flow (Flow 79; Table 1) is shown. Sediment erosion is modeled using the model of Garcia and Parker (*36*) and van Rijn *et al.* (*38*). Sediment deposition is modeled following Garcia (*37*). The observed sediment mass within a flow has been derived using the Chézy approach, assuming a bed friction coefficient (C_{fb}) of 0.004.

sensitivity on very poorly constrained parameters is in line with the earlier results of Traer *et al.* (*44*). Our sensitivity analyses show that the assumed grain size, basal sediment concentration, and the clay content of the channel floor are especially important. In Fig. 5, we assumed that the grain size in the flow is equal to the average grain size in the top 30 cm of the channel floor at each mooring location, that the ratio between depth-averaged sediment concentration and basal sediment concentration is 1.6 [following experiments of Garcia (*37*)], and that the volume percentage of clay in the top 30 cm is on average 2% [following the measurements of Hage *et al.* (*6*)]. However, it is most likely that the grain size within the flow strongly varies with the location in the flow (*27*), with the front of the flow being much coarser than the tail. In addition, the basal sediment concentration is probably much larger than 1.6 times the depth-averaged sediment concentration (*2*, *45*), as assumed in the modeling framework. Last, the top 30 cm of the channel floor sediment is highly heterogeneous with a clay-rich top of 5 cm overlying 25 cm of clay-poor sandy sediment (*6*), and it is unclear whether these properties should just be averaged. The thickness of these sediment packages will also likely vary throughout the channel. Individual changes in these assumptions result in two to five times more or less sediment erosion or deposition and show that predicting sediment transport in turbidity currents is still extremely challenging.

**A model for how flow structure evolves in space and time**
Inspection of the observed and derived flow characteristics, and how flows evolve as they move down-channel, leads us to combine our three identified flow types into sequential stages of a unified model for the down-channel evolution of turbidity current structure.

Stage 1 of this model is characterized by flows that have and maintain a dense regime head. These dense heads are high velocity, thin, and driven by high sediment concentrations. Basal friction is the dominant control on flow velocity ($C_{fb} > C_{fi}$), as the high density of the head suppresses turbulent mixing ($Ri > 0.25$) and entrainment of ambient water through the top of the flow. Where these dense heads are maintained down-channel, they bulk up through erosion of the seafloor and maintain comparable sediment concentrations but stretch (Fig. 4). The head is faster than the body; so, additional sediment required to maintain the density of the head must be supplied to the head by erosion of the seabed as it cannot be supplied from the slower-moving body. This eroded sediment can subsequently be shed backward into the trailing body as the flow stretches. Previous laboratory experiments have suggested that traction carpets may form dense layers at the base of turbidity currents (*46*, *47*). For traction carpets, sediment is supplied from above by a faster-moving turbulent cloud. However, this is the opposite of what we observe here. The observed characteristics and high Chézy-derived sediment concentrations therefore lead us to suggest that grain-to-grain interactions are likely key to maintaining the driving force of the head. This, together with the absence of an overriding turbulent layer, leads us to classify the head of these flows as modified-grain flows (*16*). Modified-grain flows [as defined by Lowe (*16*)] are gravity flows of cohesionless solids maintained in a dispersed state by an intergranular dispersive pressure arising from grain interactions within the shearing sediment but where interstitial fluid or excess pore-fluid pressure significantly aids dispersion instead of dispersion being a consequence of physical collisions alone (*1*, *16*, *48*). The flow slows behind the head and becomes dilute and increasingly

turbulent (dilute regime). Between the dense head and the dilute body, a transitional region may form where a dense near-bed layer could behave as a traction carpet. Further research is required to quantify the processes envisaged in the head of these flows and the transition to the contrasting dilute and turbulent regime that follows.

Stage 2 of the unified flow evolution model is characterized by deceleration and dilution of the head and increased mixing in the flow (Fig. 6B). Although some form of higher-velocity core is still present (Fig. 6Band Table 1), the overlying dilute cloud can now supply sediment to the dense near-bed layer behind the head. Unlike
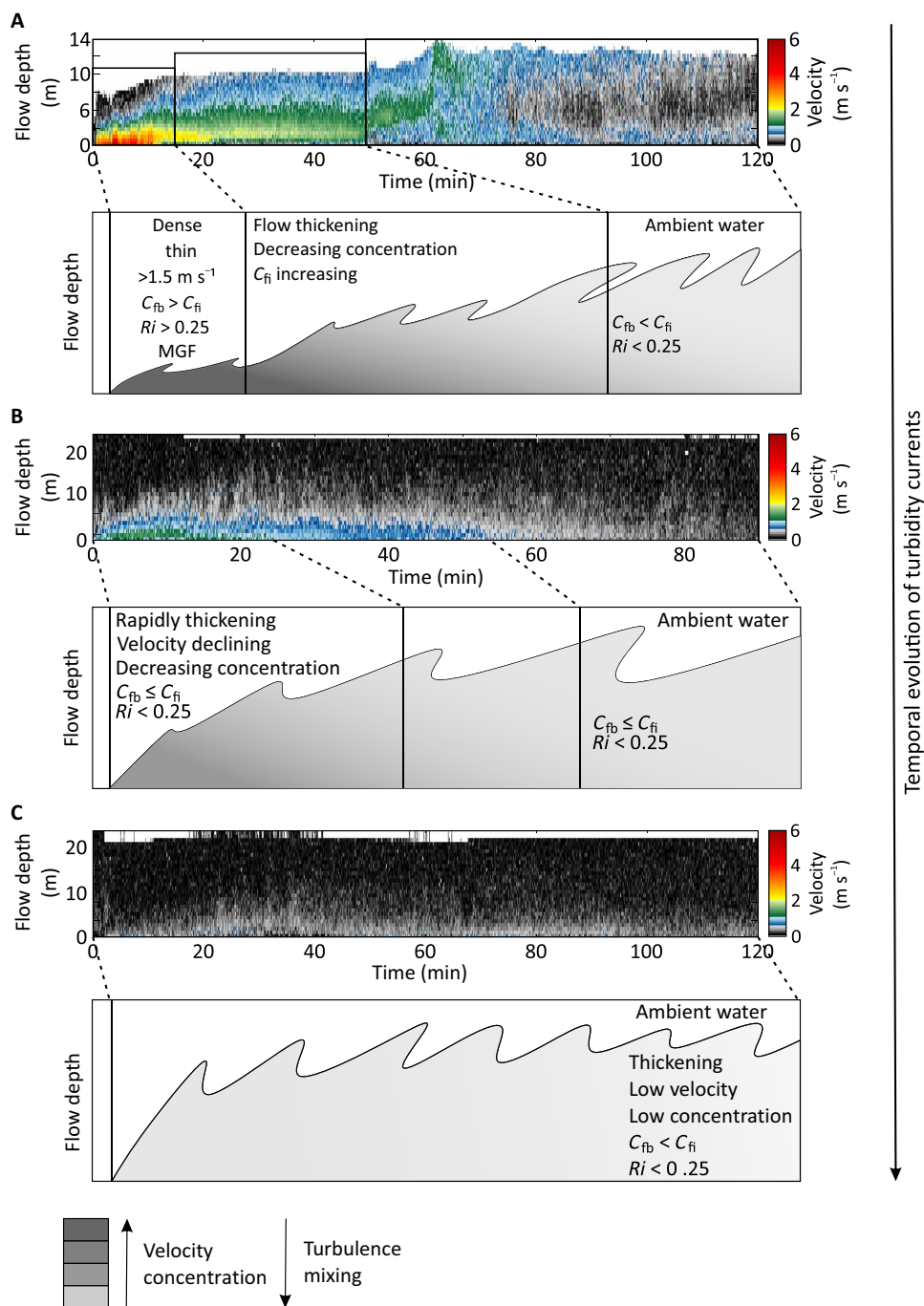
Fig. 6. Proposed turbidity current regimes and flow evolution based on Bute Inlet observations. (**A**) Turbidity current characterized initially by a fast, dense, and thin stratified head whose velocity is governed by bed friction (C_{fb}). Behind the head, the flow rapidly thickens, dilutes, and slows. The flow exhibits characteristics previously described for modified grain flows. MDF, modified grain flow. (**B**) Insufficient erosion results in dilution of the fast dense head resulting in deceleration and increased mixing. The previously dense head may now exhibit characteristics associated with a traction carpet. (**C**) The turbidity current is characterized as entirely slow, dilute, and well mixed. Behind the head of the turbidity current in (A) and the turbidity currents in (B) and (C), the exhibited characteristics more closely match those used to traditionally characterize turbidity currents.

the dense regime head in type 1 flows, this dense near-bed layer acts as a classical traction carpet (15, 49–51). The basal friction and friction at the flow-ambient water interface are more comparable in these flows ($C_{fb} \approx C_{fi}$), and the flows are mostly well mixed. Behind this higher-velocity region of the flow, the body and tail of the flow are characterized by a dilute regime.

The final stage of the unified flow evolution model is defined by flows that are entirely characterized by a dilute regime (Fig. 6C). Here, the head, body, and tail of the flows are low velocity, dilute, and well mixed ($Ri < 0.25$). Bed friction is also lower than friction between the flow and the ambient water ($C_{fb} < C_{fi}$).

Our observations of flow frequency and flow characteristics show that flow runout distance is dependent upon the ability of the flow to maintain a dense regime head. In the case of the longest runout flows that are observed, the head maintains a high density for an extended period of time (>3 hours from the Homathko Delta to M1). Fewer flows were able to maintain these dense heads, and as a result, the number of flows greatly decreases with distance. These results also show that flows may evolve through each stage of our model sequentially from initiation to dissipation.

In some circumstances, it is possible that a dense regime head will never develop. This may be the case where initial flow velocities are too low or, perhaps, when turbidity currents are triggered by hyperpycnal (plunging) river floods (52). Previous observations from the Squamish Delta, a similar fjord-head delta to Bute Inlet, have shown that turbidity currents were triggered by sediment settling from very dilute (~0.07 kg/m^3) surface river plumes. Here, the triggered turbidity current was shown to erode the seafloor and thus bulk up, similar to flows shown in Bute Inlet (53). However, erosion and runout were limited to sites close to the delta. Such flows therefore appear to have not developed the dense head regime identified in the longest runout events in Bute Inlet. Nonetheless, if sufficient erodible sediment had been available, then it is entirely plausible that continued erosion may have resulted in the development of a dense regime head as has also been observed for other flows at Squamish (54). Stages 2 and 3 of our model therefore appear to describe the less erosive turbidity currents observed on the Squamish Delta and their evolution (22, 53, 54). Because of this and other observations of dilute events, the model seems appropriate for describing turbidity currents previously characterized by dilute turbulence-dominated models including those that fail to develop a denser head (14, 46, 47). Nevertheless, future work should focus on understanding the transformation of the initially triggered flow mass into a longer runout turbidity current.

Preservation of turbidity current characteristics in deposits

Our generalized model for turbidity current structure and evolution that is based on direct field observations may explain features commonly reported in turbidity current deposits (turbidites). Although we are unable to directly link the monitored flows to their exact deposits, sediment cores recovered from the submarine channel in Bute Inlet and previously deployed sediment traps reveal a similar structure to turbidity current deposits in those prior studies (6, 40, 55). Deposits from high-density parts of turbidity currents have been proposed to consist of coarser grained deposits, which lack cross-stratification. These deposits are commonly characterized by T_A, T_{B-2}, and T_{B-3} divisions from the Bouma sequence (15, 56, 57). The lack of cross-stratification is a consequence of the high sediment concentrations, suppressing turbulence and favoring rapid

deposition (58, 59). Box cores and piston cores along the channel thalweg and on the lobe contained turbidites with characteristic massive sands (T_A) at their base (6, 40, 55), and we propose that these deposits relate to the dense flow regime head.

These coarse basal deposits are typically overlain by finer-grained intervals, some of which have evidence of cross-stratification (T_{B-1}, T_C, T_D and/or overlain by T_E) indicative of dilute sediment concentrations and slower rates of deposition (15, 18). Above the T_A division, turbidites cored from the channel in Bute Inlet are fine-grained, exhibiting cross-laminations and capped by thin mud and silt deposits (T_E) (6). Sediment traps suspended above the channel thalweg (located 5 and 32 km from the Homathko Delta) also captured discrete coarser sands separated by discrete mud layers (40, 55). We propose that these cross-laminated and finer-grained deposits relate to the more dilute regime flows, primarily emplaced from the body and tail of flows.

Linking the observed flow regimes with characteristic deposits may also explain bimodality in turbidite thickness. Detailed studies of ancient turbidite successions identified that thin (<40 cm thick) finer-grained beds (T_{B-1}, T_C, T_D, and/or T_E divisions related to dilute flows) are more common, while coarse beds thicker than 40 cm (T_A, T_{B-2}, or T_{B-3} divisions related to dense flows) are rarer (15, 57, 58). The thinner finer-grained beds are also more common in locations further from source (57, 58, 60). Our data appear to support these interpretations, as we see a much greater frequency of dilute flows, which likely emplace thinner, finer-grained deposits. Dense flows are also shown to transport the most sediment and are therefore likely to produce the thicker deposits. Our data also indicate that the higher-velocity, denser flows are more prone to long-distance runout than dilute flows; hence, we suggest that this may explain why characteristic coarse sand beds can be tracked out over tens to hundreds of kilometers (57, 60, 61). Further direct monitoring and sampling studies should aim to directly link individual deposits with the flow that formed them to enhance the link between geological archives and the processes that form them.

Common characteristics of particle-laden gravity flows

A need for more detailed monitoring along the length of field-scale flows is not unique to turbidity currents. Our understanding of other hazardous particle-laden flows on land, such as pyroclastic density currents and powder snow avalanches, is similarly constrained by a paucity of direct observations and measurements due to the unpredictability of these flows, their tendency to damage equipment, and their opacity (62–64), although there have been recent advances such as snow avalanche test sites (65). The sparse number of detailed direct measurements hampers modeling of the potential hazards from all of these flow types, and thus adoption of appropriate mitigation strategies. Although there are some fundamental differences between turbidity currents, snow avalanches, and pyroclastic flows, it is also useful to compare them and determine whether common aspects or modes of behavior exist. This comparison may also aid the design of future marine field experiments that give wider insights into the physics of particle-laden flows and inform numerical modeling.

Particle-laden gravity flow model accuracy is governed by the choice of appropriate flow laws, i.e., whether the flow is dilute, turbulent, and well mixed, or dense where grain-to-grain interactions dominate and the flow remains stratified (62). Both regimes have fundamentally different dominant physical processes. Turbidity

currents, pyroclastic density currents, and snow avalanches will differ in many characteristics, such as absolute velocities due to the density contrasts with the ambient fluid through which they travel, settling velocities of grains, how grains are held aloft (e.g., by grain interactions versus fluid turbulence), or the slope angles over which they flow (65, 66). Pyroclastic density currents are also likely to have larger particle-size distributions and additional buoyancy effects owing to their thermal characteristics (67), while snow avalanche dynamics are impacted by particle sizes ranging over orders of magnitude (53), the temperature of the snow, and the ability of particles to (dis)aggregate (68).

Nonetheless, our data suggest that similar flow regimes may potentially exist across different flow phenomena. For example, closely behind the fronts (heads) of stratified pyroclastic flows and powder snow avalanches, grain-to-grain interactions within a dense flow region have been characterized to dominate particle transport behavior (64, 66, 69, 70). These characteristics are similar to those envisaged for the dense regime heads of our observed type 1 flows (Fig. 6A). Behind these dense regions, the upper parts of pyroclastic flows and snow avalanches may often comprise expanded, turbulent, and dilute particle suspensions as a consequence of air resistance and ingestion with denser parts of the flow existing at the bed (65, 70, 71). In our data, we also observe this transition as increasing volumes of water are entrained and the flow becomes increasingly well mixed (Fig. 6A). Pyroclastic surges and air-borne snow avalanches are entirely dilute with characteristics similar to the body and tail of our observed type 1 and type 2 flows and the entirety of our type 3 flows (72–74). As in our model for turbidity current evolution, air-borne snow avalanches also originate from denser flows, which have created a suspension layer, but where the dense flow has stopped first because of higher friction in its core, leaving the suspension layer to continue to flow. This comparison therefore suggests that simulating all three phenomena requires a multiregime modeling approach with particular focus on high-concentration regimes in the head of the flow.

A third flow regime has also been identified for pyroclastic density currents and powder snow avalanches (70, 75). This regime is termed an intermediate flow regime, for pyroclastic flows, or in the case of snow avalanches has been referred to as the intermittency region, intermediate flow regime, or the fluidized regime. Here, both particle-particle and particle-fluid interactions play a key role in the mass balance between the dense basal layer and the overlying turbulent suspension (63, 70, 75). However, although likely, it is unclear from our data whether the observed turbidity currents in Bute Inlet have a similar intermediate flow regime. This is because the ADCPs do not provide direct density measurements such as those that have been made in the other flow types to identify these characteristics. Identification and quantification of the characteristics of this flow regime, either through field observations or laboratory experiments, should therefore be a priority as its presence would likely play a major role in the transition between type 1 and type 3 turbidity currents.

Comparisons of runout distance can be readily made between flow types. Our turbidity current observations show that runout is enhanced if the flow can maintain a dense regime head. These seabed flows were shown to bulk up by up to three orders of magnitude as they eroded the substrate along the channel, thereby sustaining this dense frontal area (Fig. 4). Field and modeling studies have shown that snow and substrate entrainment is also a key control on snow avalanche and pyroclastic density current runout (68, 74, 76–79); the majority of snow entrainment also occurs beneath the faster

denser head (80). However, in both snow avalanches and pyroclastic density currents, mass increase does not normally exceed an order of magnitude. This may be a function of shorter runout distances where mass balance estimates of snow avalanche and pyroclastic density currents have been made, the availability of erodible substrate or their greater particle settling velocities compared to turbidity curents. It is therefore clear that to model and capture the behavior of these flows, appropriate erosion relationships are needed, which take into account different flow regimes and appropriate detrainment relationships.

Definition of an appropriate flow regime is, however, only the first step for modeling turbidity current erosion and entrainment. Observations of powder snow avalanches have revealed multiple mechanisms for entraining snow, including ploughing and scouring (81, 82). These mechanisms have different rates of entrainment and act over different temporal and spatial scales within the flow and affect the amount of energy required to fully entrain material (65, 80). Quantifying the relative importance of different seabed erosion mechanisms [i.e., liquefaction and scour (16, 83, 84)] and where those mechanisms occur in seafloor turbidity currents is therefore a key future goal.

Summary and wider implications

Direct monitoring in Bute Inlet shows the presence of contrasting dense and dilute turbidity current regimes, leading to a new generalized turbidity current evolution model (Fig. 6). These observations suggest that turbidity currents can often be composed of heterogeneous flow regimes (Fig. 6). Where monitoring of turbidity currents in other submarine canyon and channel locations has been carried out, such as Congo Canyon (23, 27), Monterey Canyon (2, 26), Howe Sound (22, 53), and Pointe-des-Monts (24), the observation of faster flows with, and slower flows without, dense basal layers supports this general model of flow evolution in both muddy and sandy systems. However, more observations from a wider range of environmental settings, i.e., muddy or carbonate systems, are required to determine the universality of the model. Nevertheless, this model has major implications for geohazards, as a dense high-velocity head, if present, will have considerably higher impact forces than dilute flows. Erosion and lowering of the bed of submarine canyons and channels by this head as it traverses a submarine system may also increase the risk of seafloor infrastructure damage. Sediment fluxes derived from ADCP measurements also suggest that fast, dense heads dominate fluxes through submarine channel systems. These heads therefore disproportionately control the amount of reworking and residence times of sediment, pollutants, and organic carbon within these systems before these particles are deposited within the lobe at the end of the system. By determining the flux of material through these systems, they also likely control the long-term evolution of submarine channel systems and their geomorphology and sedimentology.

MATERIALS AND METHODS
ADCP data collection
An array of six moorings were deployed along the submarine channel in Bute Inlet at water depths of 180 to 610 m (85). The four shallowest moorings (180 to 470 m) were two-point moorings, i.e., instruments suspended between two anchors placed on either side of the channel [see (85) for full details], and were deployed from the

RV John Strickland. Previous single-point (suspended from single anchors that were located within the channel) ADCP moorings in Monterey Canyon and Congo Canyon have been found to be impacted by turbidity currents in terms of being pulled down, pitching, rolling, and rotating (*2*, *85*). This affected the data quality, particularly during the passage of the initial faster head of the flow as the stress on the mooring chain was greatest. By suspending the ADCP from anchors on either side of the channel axis, the ADCPs interacted less with the flow than in other studies using only single-point moorings. This improved the data quality, particularly at the start of the flows, as the ADCPs did not suffer from the abrupt pull-down experienced in other studies (*2*). The ADCPs were also able to correct for any rotation because of their internal compasses. The two deepest (560–610 m) were single-point moorings and were deployed from the *CCGS Vector*. Despite being single-point moorings, the ADCPs did not appear to suffer pull-down seen elsewhere when impacted by the long runout flow. They did experience a couple degrees of roll; however, the ADCP measurements were not affected by sidewall echo (*85*) because of their placement in the center of channel (M2) and on the channel lobe (M1). These moorings were deployed in 2018 for 206 days between 15 May and 8 November. The upstream mooring was placed 2880 m down-channel of the Homathko River Delta. The furthest downstream mooring was placed 43,800 m (along the channel thalweg) from this delta on the channel lobe. Downward-looking ADCPs with frequencies of 300 to 600 kHz were suspended from the moorings at heights of ~8 to ~30 m above the channel floor (table S1). The ADCPs measured profiles of velocity and acoustic backscatter at vertical and temporal resolutions of 0.5 to 1 m and 4 to 6 s, respectively (table S1). ADCPs on all moorings recorded throughout the 206 days except M5, which failed to record because of the instrument flooding during its initial deployment.

Flow velocities, durations, and discharges

Turbidity currents were identified in the ADCP data based on sudden increases in down-channel velocity and increased backscatter (indicative of suspended sediment) within the water column (*2*, *86*). Transit velocities were calculated using arrival times at sequential moorings and the down-channel distance between moorings along the channel thalweg (*26*).

Flow duration and total discharge (i.e., sediment and water) were calculated for each turbidity current at each mooring. Flows were defined to have ended when velocities beneath the ADCP returned to background rates below the ADCP (table S2). Background velocity was used rather than acoustic backscatter because of sediment often remaining suspended in the water column for a considerable length of time after a significant down-channel velocity signal was undetectable. Total discharge volumes were calculated by time-integrating the measured turbidity current velocities multiplied by the channel cross-sectional area. As no channel was present at M1 (Fig. 1), because of its lobe location, a width 0.5 times the total inlet width was used (table S1).

Other turbidity current characteristics

To understand how a turbidity current evolves and what drives this evolution, additional flow characteristics needed to be derived. Principally, sediment concentration (i.e., what drives the flow), bulk Richardson numbers (i.e., the degree of mixing in the flow), and the balance between friction at the top of the flow and the bottom of the flow needed to be derived. Here, to derive these variables, we used iteratively solved, modified Chézy equations (*31*, *32*). The Chézy approach is commonly used in rivers but has previously been used to analyze turbidity current characteristics (*31*, *47*, *87*, *88*) and defines the relationship between flow speed, the gravitational driving force, and the resistive force of friction (*33*). However, unlike rivers, application of this approach to turbidity currents also requires a consideration of friction between the ambient water and the top of the flow (*31*). It should also be noted that the Chézy approach defines a balance for the forces at a measurement location and does not take into account inherited momentum from upstream. For example, upstream of the measurement location, the turbidity current may flow over a locally steeper section of channel, such as a knickpoint, which will result in the acceleration of the flow. It will therefore be traveling at a greater velocity than it would have been with a consistent slope gradient similar to that at the measurement site. For the flow to be in balance with the channel at the measurement site according to the Chézy approach, the Chézy approach would therefore predict higher sediment concentrations, which would be needed to sustain the higher observed velocities over the lower slope gradient.

First, depth-averaged flow velocities (*U*) and flow height (*H*) were calculated using the measured ADCP velocity data following the integral approach of Ellison and Turner (*89*). The seabed reflector was obscured during the passage of the heads of some of the faster flows in the ADCP data, resulting in a blanking zone. This is a consequence of the attenuation of acoustic energy by the densest part of the flow (*2*, *22*, *24*). Where this occurred, the base of the flow was defined as the deepest retrieved velocity measurement, although the base was likely a couple of meters below this, and thus, the flow head was slightly thicker than input into the Chézy calculations. Despite this, the highest velocity measurements retrieved were obtained directly above the blanking zone and subsequently decayed with height. It is therefore likely that the depth-averaged velocities that were used underestimated the actual depth-averaged velocity of the faster flow heads. The depth-averaged sediment concentrations in these parts of the faster flows are therefore likely greater than reported here. The depth-averaged sediment concentration was subsequently calculated

$$U^2 = \frac{1}{C_{\text{fi}} + C_{\text{fb}}} RCgHS \tag{1}$$

where C_{fb} is the bottom friction coefficient, R is submerged specific gravity of the sediment, taken here to be the value for quartz (~1.65), g is the gravitational acceleration, S is the slope gradient at the mooring (table S1), and the friction on the top interface (C_{fi}) of the fluid is calculated using

$$C_{\text{fi}} = \frac{0.0075}{\sqrt{1 + 718\,Ri^{2.4}}}(1 + 0.5Ri) \tag{2}$$

and following Parker *et al.* (*32*), setting the bulk Richardson number (*Ri*) to

$$Ri = \frac{RgCH}{U^2} \tag{3}$$

To make these calculations, we follow Konsoer *et al.* (*31*) and assume that the bottom friction coefficient (C_{fb}) should be between 0.002 and 0.006. Simmons *et al.* (*27*) estimated the bed roughness of the Congo Canyon to be ~0.002. However, we continue to use 0.002 to 0.006 because of the potentially rougher seabed resulting from the sandier substrate and the widespread presence of seafloor

bedforms ([90], [91]). This decision ignores the possibility that the erosive nature of the turbidity current can also affect the bed roughness. Where turbidity currents are able to erode the seabed and generate scours, these scours should work to slow the eroding current as would be predicted by hydraulic relationships showing that average flow velocities and bed roughness are inversely related ([92]). However, given that turbidity current velocity is related to sediment volume, this relationship may break down if sufficient volume is eroded despite the bed roughness increase ([92]–[95]). This relationship is further complicated during the passage of the flow as the body and tail may be less erosive and thus interacting with the bed roughness surface generated by the more erosive head of the flow ([23]). As a consequence of this complication, we choose to assume a constant bed roughness value throughout the flow despite erosive flows potentially generating rougher beds. The seafloor slope in each calculation is directly measured from bathymetry beneath the ADCP.

Comparing observations with sediment transport models

We compare the down-channel evolution of the sediment mass transported within the most powerful flow with the evolution predicted by some of the most commonly used sediment transport models. We model erosion using the models of Garcia and Parker ([36]) and van Rijn et al. ([38]).

The mass flux of sediment per square meter of channel floor per second entrained into the turbidity current (F_s) is first modeled here following Garcia and Parker ([36])

$$F_s = E_s v_s \rho_s \qquad (4)$$

where E_s is a dimensionless sediment entrainment coefficient defined as

$$E_s = \frac{A_{\mathrm{Garcia}} Z_u^5}{1 + A_{\mathrm{Garcia}}/0.3\, Z_u^5} \qquad (5)$$

where A_{Garcia} is set to 1.3×10^{-7}, and Z_u is defined as

$$Z_u = \frac{u_*}{v_s} Re_p^{0.6} \qquad (6)$$

where u_* is the bed shear velocity, v_s is the terminal fall velocity, and Re_p is the particle Reynolds number. Here, we estimate the fall velocity using Budryck's equation

$$v_s = \frac{0.008925}{d_{50}} \left(\sqrt{1 + 95\frac{\rho_s - \rho_w}{\rho_w}(1000 * d_{50})^3} - 1 \right) \qquad (7)$$

where d_{50} is the median grain size, ρ_w is the density of seawater (here set to 1028 kg/m^3), and ρ_s is the density of the sediment (here set to 2650 kg/m^3). The grain size (d_{50}) is vertically averaged over the top 0.3 m of the channel fill deposits as sampled by Hage et al. ([6]) for each of the individual mooring sites. The particle Reynolds number is defined as

$$Re_p = \frac{\sqrt{Rg}\, d_{50}^{1.5}}{\upsilon} \qquad (8)$$

where R is the submerged specific gravity ($\rho_s/\rho_w - 1$), g is the gravitational acceleration, and ν is the kinematic viscosity of seawater at 4°C (1.6×10^{-6}). The bed shear velocity is set to $u_* = \sqrt{\frac{\tau}{\rho_w}}$ by definition, and the shear stress is calculated as

$$\tau = \rho_w g \left(\frac{U}{C_h'} \right)^2 \qquad (9)$$

where U is the depth-averaged flow velocity taken from the ADCP instruments, and C_h' is the Chézy coefficient following van Rijn et al. ([38])

$$C_h' = 5.75 \sqrt{g} \log\left(\frac{12H}{3\, d_{90}} \right) \qquad (10)$$

where H is the flow depth measured by the ADCP, and d_{90} is the sediment grain size at the 90th percentile of the channel floor sediment here set to three times the d_{50}.

van Rijn et al. ([38]) provide a second erosion model, where the mass flux of sediment per square meter of channel floor per second entrained into the flow is defined as

$$F_s = 0.00033\, \rho_s \sqrt{\frac{\rho_s}{\rho_w} g\, d_{50}}\, D_*^{0.3} \left(\frac{\theta - \theta_{cr,d}}{\theta_{cr,d}} \right)^{1.5} \qquad (11)$$

where D_* is the dimensionless grain size parameter defined as

$$D_* = d_{50} \sqrt[3]{\frac{\left(\frac{\rho_s}{\rho_w} - 1\right)g}{\upsilon^2}} \qquad (12)$$

and θ is the Shield's parameter defined as

$$\theta = \frac{\tau}{\left(\frac{\rho_s}{\rho_w} - 1\right)g\, d_{50}} \qquad (13)$$

The critical Shield's parameter is defined as ([96])

$$\theta_{cr,d} = \theta_{cr} \left[1 + \frac{A_{\mathrm{Rhee}}}{\frac{\rho_s}{\rho_w} - 1} \frac{v_e}{k} \frac{n_{sl} - n_i}{1 - n_{sl}} \right] \qquad (14)$$

Here, θ_{cr} is set to 0.04 following Shields (1936), A_{Rhee} is set to 1.3 following van Rhee ([96]), and k is the permeability in meters per second, We use the permeability values reported in Foortse et al. ([97]) for their 2% clay experiments, and we interpolate between their two d_{50} values to match the d_{50} observed in the Bute Inlet channel floor samples. We set the porosity values of the sheared layer (n_{sl}) and the in situ bed value (n_i) to 0.45 and 0.4, respectively. v_e is the velocity with which the bed level is reduced during erosion, which is here estimated as $v_e = \frac{F_s}{\rho_s(1 - n_i)}$ and obtained iteratively.

The mass flux of deposition to the bed per square meter of the channel floor per second is here modeled using the equation of Garcia ([37])

$$D_s = v_s r_0 C \rho_s \qquad (15)$$

where r_0 is set to 1.6, and C is the depth-averaged sediment concentration derived from the Chézy equation.

We then convert the sediment fluxes per square meter of the channel floor per second to changes in megatons of sediment in the flow between moorings. We first interpolate the flows into a time series of 10,000 measurements. We then calculate the footprint (A_{fp}) of each individual measurement

$$A_{fp} = U \Delta T \, W_{channel} \tag{16}$$

where ΔT is the time interval in between the 10,000 individual measurements, and $W_{channel}$ is the channel width set to 130 m at M6, 325 m at M4, 300 m at M3, 226 m at M2, and 500 m at M1. In sequence, footprints are then averaged between the upstream and the downstream mooring to estimate the average footprint of that 1/10,000 slice of the turbidity current while traveling between the moorings. The average footprint is multiplied by the travel time in between the moorings to estimate the total flux of sediment in or out of the flow. The travel time is calculated by dividing the distance in between the moorings (9.2 km from M6 to M4, 15.79 km from M4 to M3, 7.82 km from M3 to M2, and 8.11 km from M2 to M1) by the average velocity between the two moorings for that slice of turbidity current. After multiplying the erosion and deposition rates by the average footprint and the travel time, the final values are divided by 10^9 to convert from kilograms to megatons.

SUPPLEMENTARY MATERIALS

REFERENCES AND NOTE

1. G. V. Middleton, M. A. Hampton, Part I. Sediment gravity flows: Mechanics of flow and deposition, in *Turbidity and Deep Water Sedimentation* G. V. Middleton, A. H. Bouma, Eds. (1973), *SEPM, Pacific Section, Short Course Lecture Notes*, pp. 1–38.

2. C. K. Paull, P. J. Talling, K. L. Maier, D. R. Parsons, J. Xu, D. W. Caress, R. Gwiazda, E. M. Lundsten, K. Anderson, J. P. Barry, M. Chaffey, T. O'Reilly, K. J. Rosenberger, J. A. Gales, B. Kieft, M. McGann, S. M. Simmons, M. McCann, E. J. Sumner, M. A. Clare, M. J. Cartigny, Powerful turbidity currents driven by dense basal layers. *Nat. Commun.* **9**, 4114 (2018).

3. U. Fernandez-Arcaya, E. Ramirez-Llodra, J. Aguzzi, A. L. Allcock, J. S. Davies, A. Dissanayake, P. Harris, K. Howell, V. A. I. Huvenne, M. Macmillan-Lawler, J. Martín, L. Menot, M. Nizinski, P. Puig, A. A. Rowden, F. Sanchez, I. M. J. Van den Beld, Ecological role of submarine canyons and need for canyon conservation: A review. *Front. Mar. Sci.* **4**, 5 (2017).

4. I. A. Kane, M. A. Clare, Dispersion, accumulation, and the ultimate fate of microplastics in deep-marine environments: A review and future directions. *Front. Earth Sci.* **7**, 80 (2019).

5. V. Galy, C. France-Lanord, O. Beyssac, P. Faure, H. Kudrass, F. Palhol, Efficient organic carbon burial in the Bengal fan sustained by the Himalayan erosional system. *Nature* **450**, 407–410 (2007).

6. S. Hage, V. V. Galy, M. J. B. Cartigny, S. Acikalin, M. A. Clare, D. R. Gröcke, R. G. Hilton, J. E. Hunt, D. G. Lintern, C. A. McGhee, D. R. Parsons, C. D. Stacey, E. J. Sumner, P. J. Talling, Efficient preservation of young terrestrial organic carbon in sandy turbidity-current deposits. *Geology* **48**, 882–887 (2020).

7. O. E. Sequeiros, M. Bolla Pittaluga, A. Frascati, C. Pirmez, D. G. Masson, P. Weaver, A. R. Crosby, G. Lazzaro, G. Botter, J. G. Rimmer, How typhoons trigger turbidity currents in submarine canyons. *Sci. Rep.* **9**, 9220 (2019).

8. L. Carter, R. Gavey, P. J. Talling, J. T. Liu, Insights into submarine geohazards from breaks in subsea telecommunication cables. *Oceanography* **27**, 58–67 (2014).

9. L. F. Pratson, B. J. Coakley, A model for the headward erosion of submarine canyons induced by downslope-eroding sediment flows. *Geol. Soc. Am. Bull.* **108**, 225–234 (1996).

10. M. E. Deptuck, G. S. Steffens, M. Barton, C. Pirmez, Architecture and evolution of upper fan channel-belts on the Niger Delta slope and in the Arabian Sea. *Mar. Pet. Geol.* **20**, 649–676 (2003).

11. D. Vendettuoli, M. A. Clare, J. E. Hughes Clarke, A. Vellinga, J. Hizzet, S. Hage, M. J. B. Cartigny, P. J. Talling, D. Waltham, S. M. Hubbard, Daily bathymetric surveys document how stratigraphy is built and its extreme incompleteness in submarine channels. *Earth Planet. Sci. Lett.* **515**, 231–247 (2019).

12. J. E. Hughes Clarke, A. N. Shor, D. J. W. Piper, L. A. Mayer, Large-scale current-induced erosion and deposition in the path of the 1929 Grand Banks turbidity current. *Sedimentology* **37**, 613–629 (1990).

13. D. J. W. Piper, P. Cochonat, M. L. Morrison, The sequence of events around the epicentre of the 1929 Grand Banks earthquake: Initiation of debris flows and turbidity current inferred from sidescan sonar. *Sedimentology* **46**, 79–97 (1999).

14. G. Shanmugam, High-density turbidity currents; are they sandy debris flows? *J. Sediment. Res.* **66**, 2–10 (1996).

15. D. R. Lowe, Sediment gravity flows: II depositional models with special reference to the deposits of high-density turbidity currents. *J. Sediment. Res.* **52**, 279–297 (1982).

16. D. R. Lowe, Grain flow and grain flow deposits. *J. Sediment. Res.* **46**, 188–199 (1976).

17. B. C. Kneller, M. J. Branney, Sustained high-density turbidity currents and the deposition of thick massive sands. *Sedimentology* **42**, 607–616 (1995).

18. P. J. Talling, D. G. Masson, E. J. Sumner, G. Malgesini, Subaqueous sediment density flows: Depositional processes and deposit types. *Sedimentology* **59**, 1937–2003 (2012).

19. P. J. Talling, On the triggers, resulting flow types and frequencies of subaqueous sediment density flows in different settings. *Mar. Geol.* **352**, 155–182 (2014).

20. P. H. Kuenen, Turbidity currents of high density, in *18th International Geological Congress (1948), London* (1950), vol. 8, pp. 44–52.

21. B. C. Kneller, C. Buckee, The structure and fluid mechanics of turbidity currents: A review of some recent studies and their geological implications. *Sedimentology* **47**, 62–94 (2000).

22. J. E. Hughes Clarke, First wide-angle view of channelized turbidity currents links migrating cyclic steps to flow characteristics. *Nat. Commun.* **7**, 11896 (2016).

23. M. Azpiroz-Zabala, M. J. B. Cartigny, P. J. Talling, D. R. Parsons, E. J. Sumner, M. A. Clare, S. M. Simmons, C. Cooper, E. L. Pope, Newly recognized turbidity current structure can explain prolonged flushing of submarine canyons. *Sci. Adv.* **3**, e1700200 (2017).

24. A. Normandeau, D. Bourgault, U. Neumeier, P. Lajeunesse, G. St-Onge, L. Gostiaux, C. Chavanne, Storm-induced turbidity currents on a sediment-starved shelf: Insight from direct monitoring and repeat seabed mapping of upslope migrating bedforms. *Sedimentology* **67**, 1045–1068 (2020).

25. G. Parker, Y. Fukushima, H. M. Pantin, Self-accelerating turbidity currents. *J. Fluid Mech.* **171**, 145–181 (1986).

26. C. J. Heerema, P. J. Talling, M. J. Cartigny, C. K. Paull, L. Bailey, S. M. Simmons, D. R. Parsons, M. A. Clare, R. Gwiazda, E. Lundsten, K. Andersen, K. L. Maier, J. P. Xu, E. J. Sumner, K. Rosenberger, J. Gales, M. McGann, L. Carter, E. Pope, M. C. C. E. C. Team, What determines the downstream evolution of turbidity currents? *Earth Planet. Sci. Lett.* **532**, 116023 (2020).

27. S. M. Simmons, M. Azpiroz-Zabala, M. J. B. Cartigny, M. A. Clare, C. Cooper, D. R. Parsons, E. L. Pope, E. J. Sumner, P. J. Talling, Novel acoustic method provides first detailed measurements of sediment concentration structure within submarine turbidity currents. *J. Geophys. Res. Oceans* **125**, e2019JC015904 (2020).

28. F. P. Shepard, P. A. McLoughlin, N. F. Marshall, G. G. Sullivan, Current-meter recordings of low-speed turbidity currents. *Geology* **5**, 297–301 (1977).

29. R. A. Bagnold, Experiments on a gravity-free dispersion of large solid spheres in a Newtonian fluid under shear. *Proc. R. Soc. Lond. Ser. A* **225**, 49–63 (1954).

30. J. P. Xu, O. E. Sequeiros, M. A. Noble, Sediment concentrations, flow conditions, and downstream evolution of two turbidity currents, Monterey Canyon, USA. *Deep-Sea Res. I Oceanogr. Res. Pap.* **89**, 11–34 (2014).

31. K. Konsoer, J. Zinger, G. Parker, Bankfull hydraulic geometry of submarine channels created by turbidity currents: Relations between bankfull channel characteristics and formative flow discharge. *J. Geophys. Res. Earth* **118**, 216–228 (2013).

32. G. Parker, M. Garcia, Y. Fukushima, W. Yu, Experiments on turbidity currents over an erodible bed. *J. Hydraul. Res.* **25**, 123–147 (1987).

33. P. D. Komar, Computer simulation of turbidity current flow and the study of deep-sea channels and fan sedimentation, in *The Sea; Ideas and Observations on Progress in the Study of the Seas* (John Wiley, 1977), vol. 6, pp. 603–621.

34. P. D. Komar, The channelized flow of turbidity currents with application to Monterey deep-sea fan channel. *J. Geophys. Res.* **74**, 4544–4558 (1969).

35. M. W. Stacey, A. J. Bowen, The vertical structure of density and turbidity currents: Theory and observations. *J. Geophys. Res. Oceans* **93**, 3528–3542 (1988).

36. M. Garcia, G. Parker, Experiments on the entrainment of sediment into suspension by a dense bottom current. *J. Geophys. Res. Oceans* **98**, 4793–4807 (1993).

37. M. H. Garcia, Depositional turbidity currents laden with poorly sorted sediment. *J. Hydraul. Eng.* **120**, 1240–1263 (1994).

38. L. C. van Rijn, R. Bisschop, C. van Rhee, Modified sediment pick-up function. *J. Hydraul. Eng.* **145**, 06018017 (2019).

39. B. D. Bornhold, P. Ren, D. B. Prior, High-frequency turbidity currents in British Columbia fjords. *Geo-Mar. Lett.* **14**, 238–243 (1994).

40. D. B. Prior, B. D. Bornhold, W. J. Wiseman, D. R. Lowe, Turbidity current activity in a British Columbia fjord. *Science* **237**, 1330–1333 (1987).

41. J. P. M. Syvitski, K. W. Asprey, D. A. Clattenburg, G. D. Hodge, The prodelta environment of a fjord: Suspended particle dynamics. *Sedimentology* **32**, 83–107 (1985).

42. J. P. M. Syvitski, G. E. Farrow, Structures and processes in bayhead deltas: Knight and Bute Inlet, British Columbia. *Sediment. Geol.* **36**, 217–244 (1983).

43. M. A. Clare, J. E. Hughes Clarke, P. J. Talling, M. J. B. Cartigny, D. G. Pratomo, Preconditioning and triggering of offshore slope failures and turbidity currents revealed

by most detailed monitoring yet at a fjord-head delta. *Earth Planet. Sci. Lett.* **450**, 208–220 (2016).

44. M. M. Traer, G. E. Hilley, A. Fildani, T. McHargue, The sensitivity of turbidity currents to mass and momentum exchanges between these underflows and their surroundings. *J. Geophys. Res. Earth* **117**, (2012).

45. Z. Wang, J. Xu, P. J. Talling, M. J. B. Cartigny, S. M. Simmons, R. Gwiazda, C. K. Paull, K. L. Maier, D. R. Parsons, Direct evidence of a high-concentration basal layer in a submarine turbidity current. *Deep-Sea Res. I Oceanogr. Res. Pap.* **161**, 103300 (2020).

46. G. V. Middleton, Experiments on density and turbidity currents: I. Motion of the head. *Can. J. Earth Sci.* **3**, 523–546 (1966).

47. G. V. Middleton, Experiments on density and turbidity currents: II. Uniform flow of density currents. *Can. J. Earth Sci.* **3**, 627–637 (1966).

48. G. Postma, Classification for sediment gravity-flow deposits based on flow conditions during sedimentation. *Geology* **14**, 291–294 (1986).

49. R. N. Hiscott, Traction-carpet stratification in turbidites; fact or fiction? *J. Sediment. Res.* **64**, 204–208 (1994).

50. Z. Jiang, The motion of sediment-water mixtures during intense bedload transport: Computer simulations. *Sedimentology* **42**, 935–945 (1995).

51. Y. K. Sohn, On traction-carpet sedimentation. *J. Sediment. Res.* **67**, 502–509 (1997).

52. T. Mulder, J. P. M. Syvitski, Turbidity currents generated at river mouths during exceptional discharges to the world oceans. *J. Geol.* **103**, 285–299 (1995).

53. S. Hage, M. J. B. Cartigny, E. J. Sumner, M. A. Clare, J. E. Hughes Clarke, P. J. Talling, D. G. Lintern, S. M. Simmons, R. Silva Jacinto, A. J. Vellinga, J. R. Allin, M. Azpiroz-Zabala, J. A. Gales, J. L. Hizzett, J. E. Hunt, A. Mozzato, D. R. Parsons, E. L. Pope, C. D. Stacey, W. O. Symons, M. E. Vardy, C. Watts, Direct monitoring reveals initiation of turbidity currents from extremely dilute river plumes. *Geophys. Res. Lett.* **46**, 11310–11320 (2019).

54. J. L. Hizzett, J. E. Hughes Clarke, E. J. Sumner, M. J. B. Cartigny, P. J. Talling, M. A. Clare, Which triggers produce the most erosive, frequent, and longest runout turbidity currents on deltas? *Geophys. Res. Lett.* **45**, 855–863 (2018).

55. D. B. Prior, B. D. Bornhold, M. W. Johns, Active sand transport along a fjord-bottom channel, Bute Inlet, British Columbia. *Geology* **14**, 581–584 (1986).

56. A. H. Bouma, *Sedimentology of Some Flysch Deposits: A Graphic Approach to Facies Interpretation* (Elsevier Pub. Co., 1962).

57. P. J. Talling, On the frequency distribution of turbidite thickness. *Sedimentology* **48**, 1297–1329 (2001).

58. Z. Sylvester, Turbidite bed thickness distributions: Methods and pitfalls of analysis and modelling. *Sedimentology* **54**, 847–870 (2007).

59. P. J. Talling, L. A. Amy, R. B. Wynn, New insight into the evolution of large-volume turbidity currents: Comparison of turbidite shape and previous modelling results. *Sedimentology* **54**, 737–769 (2007).

60. P. M. Sadler, Bed-thickness and grain size of turbidites. *Sedimentology* **29**, 37–51 (1982).

61. J. R. L. Allen, in *Sedimentary Structures. Their Character and Physical Basis.* (Elsevier, 1982), chap. 10, pp. 395–431.

62. J. Dufek, The fluid mechanics of pyroclastic density currents. *Annu. Rev. Fluid Mech.* **48**, 459–485 (2016).

63. G. Lube, E. C. P. Breard, T. Esposti-Ongaro, J. Dufek, B. Brand, Multiphase flow behaviour and hazard prediction of pyroclastic density currents. *Nat. Rev. Earth Environ.* **1**, 348–365 (2020).

64. A. Köhler, J. N. McElwaine, B. Sovilla, GEODAR data and the flow regimes of snow avalanches. *J. Geophys. Res. Earth* **123**, 1272–1294 (2018).

65. B. Sovilla, J. N. McElwaine, M. Y. Louge, The structure of powder snow avalanches. *Comptes Rendus Physique* **16**, 97–104 (2015).

66. M. J. Branney, B. P. Kokelaar, *Pyroclastic Density Currents and the Sedimentation of Ignimbrites: Geological Society Memoir* (Geological Society of London, 2002), pp. 1–152.

67. R. S. J. Sparks, M. Bursik, S. Carey, J. Gilbert, L. Glaze, H. Sigurdsson, A. Woods, *Volcanic Plumes* (Wiley, 1997).

68. B. Sovilla, P. Burlando, P. Bartelt, Field experiments and numerical modeling of mass entrainment in snow avalanches. *J. Geophys. Res. Earth* **111**, F03007 (2006).

69. R. S. J. Sparks, Grain size variations in ignimbrites and implications for the transport of pyroclastic flows. *Sedimentology* **23**, 147–188 (1976).

70. E. C. P. Breard, G. Lube, J. R. Jones, J. Dufek, S. J. Cronin, G. A. Valentine, A. Moebis, Coupling of turbulent and non-turbulent flow regimes within pyroclastic density currents. *Nat. Geosci.* **9**, 767–771 (2016).

71. W. B. Dade, H. E. Huppert, Emplacement of the Taupo ignimbrite by a dilute turbulent flow. *Nature* **381**, 509–512 (1996).

72. A. Voellmy, Über die Zerstörungskraft von Lawinen (on the destructive forces of avalanches). *Schweizerische Bauzeitung* **73**, 212–217 (1955).

73. J. E. Simpson, Gravity currents in the laboratory, atmosphere, and ocean. *Annu. Rev. Fluid Mech.* **14**, 213–234 (1982).

74. R. S. J. Sparks, M. C. Gardeweg, E. S. Calder, S. J. Matthews, Erosion by pyroclastic flows on Lascar Volcano, Chile. *Bull. Volcanol.* **58**, 557–565 (1997).

75. B. Sovilla, J. N. McElwaine, A. Köhler, The intermittency regions of powder snow avalanches. *J. Geophys. Res. Earth* **123**, 2525–2545 (2018).

76. J. Bernard, K. Kelfoun, J.-L. Le Pennec, S. V. Vargas, Pyroclastic flow erosion and bulking processes: Comparing field-based vs. modeling results at Tungurahua volcano, Ecuador. *Bull. Volcanol.* **76**, 1–16 (2014).

77. O. Roche, Y. Niño, A. Mangeney, B. Brand, N. Pollock, G. A. Valentine, Dynamic pore-pressure variations induce substrate erosion by pyroclastic flows. *Geology* **41**, 1107–1110 (2013).

78. D. Issler, P. Gauer, M. Schaer, S. Keller, Inferences on mixed snow avalanches from field observations. *Geosciences* **10**, 2 (2020).

79. B. Sovilla, P. Bartelt, Observations and modelling of snow avalanche entrainment. *Nat. Hazard Earth Sys.* **2**, 169–179 (2002).

80. D. Issler, Dynamically consistent entrainment laws for depth-averaged avalanche models. *J. Fluid Mech.* **759**, 701–738 (2014).

81. B. Sovilla, F. Sommavilla, A. Tomaselli, Measurements of mass balance in dense snow avalanche events. *Ann. Glaciol.* **32**, 230–236 (2001).

82. P. Gauer, D. Issler, Possible erosion mechanisms in snow avalanches. *Ann. Glaciol.* **38**, 384–392 (2004).

83. D. R. Lowe, Water escape structures in coarse-grained sediments. *Sedimentology* **22**, 157–204 (1975).

84. J. Peakall, J. L. Best, J. H. Baas, D. M. Hodgson, M. A. Clare, P. J. Talling, R. M. Dorrell, D. R. Lee, An integrated process-based model of flutes and tool marks in deep-water environments: Implications for palaeohydraulics, the Bouma sequence and hybrid event beds. *Sedimentology* **67**, 1601–1666 (2020).

85. M. A. Clare, D. G. Lintern, K. Rosenberger, J. E. Hughes Clarke, C. Paull, R. Gwiazda, M. J. B. Cartigny, P. J. Talling, D. Perera, J. Xu, D. Parsons, R. Silva Jacinto, R. Apprioual, Lessons learned from monitoring of turbidity currents and guidance for future platform designs. *Geol. Soc. Lond. Spec. Publ.* **500**, 605–634 (2020).

86. J. E. Hughes Clarke, C. R. V. Marques, D. Pratomo, Imaging active mass-wasting and sediment flows on a Fjord Delat, Squamish, British Columbia in *Submarine Mass Movements and Their Consequences*, 6th International Symposium, S. Krastal, J. H. Behrmann, D. Völker, M. Stipp, C. Berndt, R. Urgeles, J. Chaytor, K. Huhn, M. Strasser, C. B. Harbitz, Eds. (*Advances in Natural and Technological Hazards Research*, vol 37; Springer, 2014), pp. 249–260.

87. T. Mulder, J. P. M. Syvitski, K. I. Skene, Modeling of erosion and deposition by turbidity currents generated at river mouths. *J. Sediment. Res.* **68**, 124–137 (1998).

88. P. H. Kuenen, Estimated size of the Grand Banks [Newfoundland] turbidity current. *Am. J. Sci.* **250**, 874–884 (1952).

89. T. H. Ellison, J. S. Turner, Turbulent entrainment in stratified flows. *J. Fluid Mech.* **6**, 423–448 (1959).

90. J. A. Gales, P. J. Talling, M. J. B. Cartigny, J. Hughes Clarke, G. Lintern, C. Stacey, M. A. Clare, What controls submarine channel development and the morphology of deltas entering deep-water fjords? *Earth Surf. Process. Landf.* **44**, 535–551 (2019).

91. M. S. Heijnen, M. A. Clare, M. J. B. Cartigny, P. J. Talling, S. Hage, D. G. Lintern, C. Stacey, D. R. Parsons, S. M. Simmons, Y. Chen, Rapidly-migrating and internally-generated knickpoints can control submarine channel evolution. *Nat. Commun.* **11**, 1–15 (2020).

92. O. E. Sequeiros, B. Spinewine, R. T. Beaubouef, T. Sun, M. H. Garcia, G. Parker, Bedload transport and bed resistance associated with density and turbidity currents. *Sedimentology* **57**, 1463–1490 (2010).

93. J. T. Eggenhuisen, W. D. McCaffrey, P. D. W. Haughton, R. W. H. Butler, Small-scale spatial variability in turbidity-current flow controlled by roughness resulting from substrate erosion: Field evidence for a feedback mechanism. *J. Sediment. Res.* **80**, 129–136 (2010).

94. S. M. Kashefipour, M. Daryaee, M. Ghomeshi, Effect of bed roughness on velocity profile and water entrainment in a sedimentary density current. *Can. J. Civ. Eng.* **45**, 9–17 (2018).

95. P. Varjavand, M. Ghomeshi, A. H. Dalir, D. Farsadizadeh, A. D. Gorgij, Experimental observation of saline underflows and turbidity currents, flowing over rough beds. *Can. J. Civ. Eng.* **42**, 834–844 (2015).

96. C. van Rhee, Sediment entrainment at high flow velocity. *J. Hydraul. Eng.* **136**, 572–582 (2010).

97. B. Foortse, P. J. Visser, R. Bisschop, C. van Rhee, *Proceedings of the Institution of Civil Engineers-Maritime Engineering* (Thomas Telford Ltd., 2019), vol. 172, pp. 55–70.